



In-situ alloying laser powder bed fusion of Ni-Mn-Ga magnetic shape memory alloy using liquid Ga

Anastassia Milleret¹ · Ville Laitinen² · Kari Ullakko² · Nouredine Fenineche³ · Moataz M. Attallah¹

Received: 4 July 2023 / Accepted: 4 March 2024
© The Author(s) 2024

Abstract

Ni-Mn-Ga-based magnetic shape memory alloys can exhibit large magnetic field induced strains (MFIS). Recently, additive manufacturing techniques, especially laser powder bed fusion (L-PBF), have been successfully used to manufacture functional polycrystalline Ni-Mn-Ga with complex geometries, such as ‘bamboo-grained’ lattice structures. However, previous approaches of L-PBF of Ni-Mn-Ga have used pre-alloyed powders, which can limit the compositional freedom of the manufactured devices. This study explores, for the first time, the feasibility of an in-situ L-PBF alloying approach using a powder blend of elemental Ni, Mn, and Ga. Promising results were obtained despite the significant differences between the elemental Ni and Mn powders and the liquid Ga. The microstructure of the as-built sample showed distinct stripe patterns from the 14 M structure confirmed by XRD analysis. Heat-treatment significantly improved chemical homogeneity, dissolved the Ni-rich phase but couldn’t dissolve MnO hindering the shape memory effect.

Keywords Additive manufacturing · Laser powder bed fusion · Magnetic shape memory materials · In-situ alloying · Ni-Mn-Ga · Liquid Ga

1 Introduction

Ni-Mn-Ga-based magnetic shape memory (MSM) alloys have received much attention since their discovery in 1996 [1] due to their ability to exhibit large magnetic-field-induced strains (MFIS). This straining phenomenon occurs at ambient temperature due to the magnetic-field-induced reorientation of the martensite twin variants and is subsequently observable as twin boundary motion. Large MFIS

have been previously reported up to 6% [2] in five-layered modulated (5 M/10 M) martensite, 10% [3] in seven-layered modulated (7 M/14 M) martensite, and 12% [4] in (elementally-doped) non-modulated (NM) martensite. The MFIS occurs in few milliseconds making Ni-Mn-Ga alloys good candidates for micro-actuators and sensors, micropumps and energy harvesters.

Large MFIS are typically observed in single crystals [2–4] or individual grains [5], as grain boundaries impede twin boundary motion. However, previous research has demonstrated that introducing porosity to polycrystalline Ni-Mn-Ga reduces the grain boundary constraints, leading to an increase in MFIS. Research by Chmielus et al. [6] showed that using sodium aluminate as a spaceholder in a cast polycrystalline Ni-Mn-Ga foam resulted in a MFIS of 8.7%. Additive manufacturing techniques have also been employed to enhance the MSM effect in polycrystals by fabricating porous structures through binder-jetting [7–10], ink-printing [11, 12], laser-based directed energy deposition [13], and laser powder bed fusion (L-PBF) [5, 14–17]. Porous samples were achieved either by leveraging the inherent porosity created by the process, such as binder jetting, achieving 0.01% MFIS [7], or by printing lattice structures with ‘engineered porosity’ with bamboo-like grains,

✉ Anastassia Milleret
avm965@student.bham.ac.uk

✉ Ville Laitinen
ville.laitinen@lut.fi

✉ Moataz M. Attallah
m.m.attallah@bham.ac.uk

¹ School of Metallurgy and Materials, University of Birmingham, B15 2TT Edgbaston, UK

² Material Physics Laboratory, Lappeenranta-Lahti University of Technology LUT, Yliopistonkatu 34, 53850 Lappeenranta, Finland

³ ICB UMR 6303, CNRS, University of Bourgogne Franche-Comté, UTBM, F-90010 Belfort, France

where large grains spanning the diameter of the lattice struts are stacked on top of each other [18, 19]. Additionally, high texture characterised by large grains oriented in a similar direction appears to promote large MFIS [20, 21], and the presence of twins spanning the grain boundaries has been observed in previous studies [22]. Laser-based methods prove advantageous in this context, as the texture of the printed component can be carefully controlled through the adjustment of process parameters, thereby influencing the thermal gradient.

So far, the prevailing challenges in the obtention of large MFIS through additive manufacturing revolve around the chemical composition, particularly in binder-based techniques, and the presence of high residual stresses in laser-bed techniques. Notably, binder-based methods inevitably lead to contaminations from the liquid binding agent, thereby increasing the oxygen and risks of Ti contamination during sintering [10, 23], which, in turn, affects the MSM properties. Previous research on L-PBF of Ni-Mn-Ga demonstrated the feasibility of producing a functional actuator with 5.8% strain in a single grain extracted from a wall, after heat treatment [5]. This highlights that a homogenisation process at 1090 °C for 24 h, followed by an ordering treatment at 800 °C for 4 h, is sufficient to release adequate amount of residual stresses, thereby enhancing the MFIS. Despite L-PBF being identified as the most suitable process for producing ‘bamboo-grained’ lattice structures [16, 22], the challenges related to chemical composition, specifically Mn evaporation remains. Previous studies using pre-alloyed gas atomised powder have revealed that the evaporation of Mn in L-PBF Ni-Mn-Ga samples is greatly impacted by the process parameters, thus affecting the MSM effect [15, 16]. While gas atomisation is a costly process with limited composition freedom, an elemental approach, using a Ni, Mn, and Ga blend, offers greater composition freedom and can mitigate evaporation issues, modify properties, and manage microstructural development.

Various approaches to fabricate Ni-Mn-Ga compounds from elemental material have been explored by leveraging the high interdiffusion of Ni, Mn and Ga [11, 24, 25]. It has been demonstrated that Ni-Mn-Ga thin films can be achieved through electrodeposition of elemental Ni, Mn and Ga [25]. However, after annealing between 800 and 900 °C for 3 to 7 h, the thin films exhibited an inhomogeneous chemical composition with a mixture of L2₁ austenite, 10 M and NM martensite and Mn oxides. Although a higher temperature treatment might stabilise the martensite phase, the unavoidable formation of oxides (due to the process) remains detrimental to the MFIS. Zheng et al. [24] proposed a similar method using a hollow Ni tube with Mn electrodeposited on the outside and Ga added as a liquid inside the hole. After homogenisation at 1000 °C for at least 24 h, followed by

ordering at 750 °C for 12 h, one sample exhibited a single phase L2₁ structure, while the intended composition aimed for a 10 M martensite. The chemical composition varied radially but could be considered homogenous in the longitudinal direction over a short range of about 1 mm. Taylor et al. [11] also exploited the high diffusivity of Ga into Ni and Mn to create porosity through Ga voids using ink-printing additive manufacturing. They obtained samples with an homogenous chemical composition of Ni₅₀Mn₃₂Ga₁₈ (at%) after sintering at 1000 °C for 12 h, followed by ordering at 700 °C for 10 h, resulting in NM martensite. The precursor material comprised irregularly shaped Ni and Mn particles mixed with a solution of liquid Ga in a polymer binder. The resulting Ga droplets ranged from 10 to 100 µm in size, while the Ni and Mn powders were < 10 µm. This substantial difference in particle size does not seem to affect the chemical homogeneity of the final parts, likely due to the large layer thickness associated with this method, approximately 400 µm.

In the L-PBF process, using powder blends has been associated with issues such as low repeatability, unmelted powders, and segregation. The final microstructure is largely dependent on the degree of mixing and the size of the laser beam. In order to minimise composition gradients, the powder elements must be of similar melting temperatures, particle size, and flowability [26]. Despite these challenges, the use of powder blends has gained popularity for its cost-effectiveness and versatility in adjusting chemical composition, especially in the development of high entropy alloys [26, 27]. In the case of Ni-Mn-Ga, Ga’s low melting point (~30 °C) may pose difficulty in blending with other elements, but it readily forms alloys with both Ni and Mn. This study explores, for the first time, L-PBF of Ni-Mn-Ga from an elemental powder blend.

2 Experimental procedure

2.1 Powder blend

The blend was made from elemental gas atomised Ni powder, crushed Mn, and liquid Ga. The elements were blend together to obtain a composition of Ni₄₉Mn₃₁Ga₂₀ (at%) with an additional 2 at% of Mn to compensate from the typical evaporation of Mn during the L-PBF process [14, 16, 28]. The melting temperature of the purchased Ga was approximately ~30 °C, therefore the Ga was incorporated as a liquid into the blend of Ni and Mn using different steps schematised in Fig. 1. First, a bottled mixture of Ni (spherical powder)+Mn (crushed powder)+Ga (liquid) was placed onto a rotational mill for two hours, with a reheating step (up to 40 °C) every 5 min. The bottle was heated by

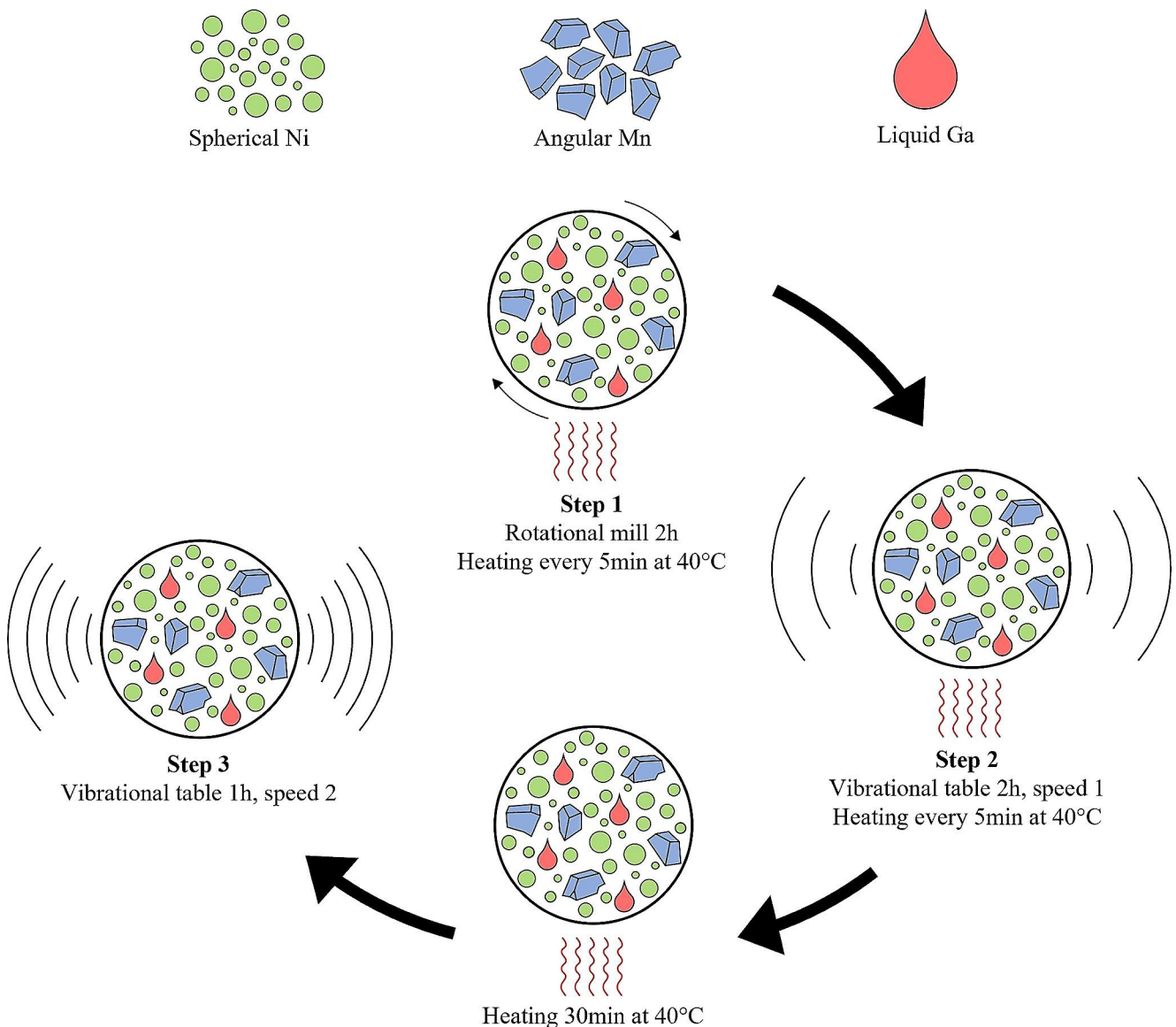


Fig. 1 Schematic diagram representing the steps during the powder blend preparation

placing in hot water during approximately 3 min and shook several times. Second, the bottle was placed on a vibrational table for two hours, with a reheating step every 5 min. Third, the bottle was heated up again at 40 °C and placed on the rotational table for an hour with a doubled vibration speed.

Scanning electron microscopy (SEM) was performed after each step using a Hitachi TM3000 microscope equipped with energy dispersive spectroscopy (EDS). Figure 2 shows a micrograph and an EDS map after each step. It is observed that a simple ball milling step leads to large Ga spherical aggregates (Fig. 2a) and low vibration leads to large plane aggregates (Fig. 2b). Only an increase of the vibration speed causes the Ga to break into smaller particles although remaining larger than the Ni and Mn ones. All

weighting and powders collection were performed inside a glovebox filled with argon atmosphere to prevent oxidation.

The particle size distribution ($d_{10}=17.51\ \mu\text{m}$, $d_{50}=49.42\ \mu\text{m}$, and $d_{90}=213.2\ \mu\text{m}$) of the blended powder was measured by laser diffraction (Sync particle analyser, Microtrac MRB) and shown in Fig. 3. The powder includes a relatively large distribution of different particle sizes. Two distinct distribution peaks are observable, the first one corresponding to the Ni and Mn particles at 39.75 μm , and the second one corresponding to Ga particles at 151.10 μm .

2.2 L-PBF process and design of experiment

L-PBF samples were fabricated using a Concept Laser M2 Cusing system, operated using a 400 W continuous-wave

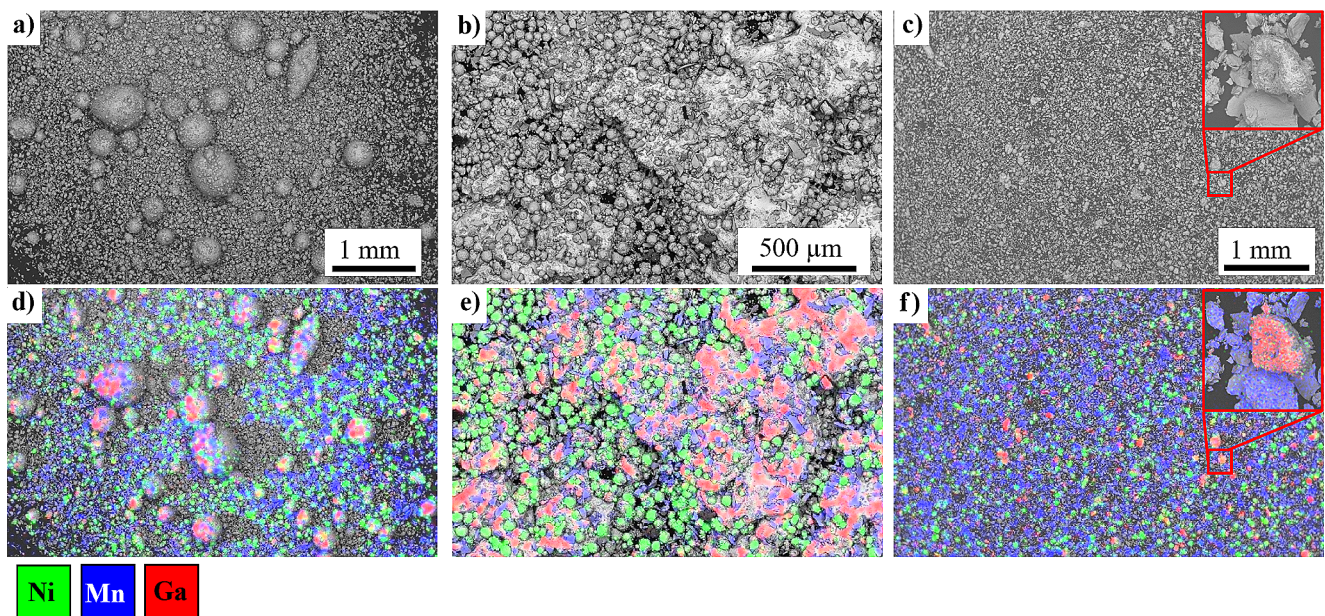


Fig. 2 SEM images of the powder blend after the (a) first, (b) second, and (c) third step, and (d, e, f) their respective EDS maps. The red outlined inset images in (c) and (f) show a Ga particle

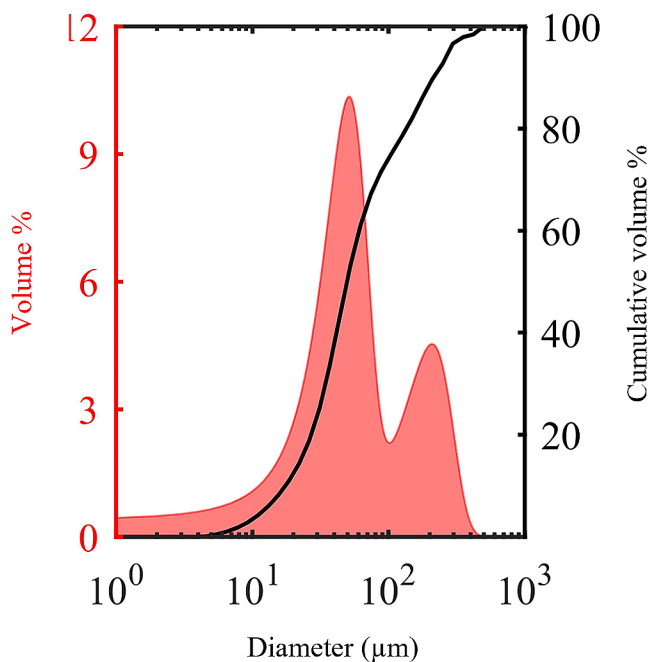


Fig. 3 Particle size distribution of the Ni-Mn-Ga powder blend

fibre laser, with a wavelength of 1.064 μm , a maximum beam speed up to 4 m/s and a fixed focus diameter of $\sim 67 \mu\text{m}$. The samples were built under a protective argon atmosphere to obtain the minimum O₂ content of 100 ppm. A unidirectional scanning strategy was adopted, as illustrated schematically in Fig. 4a, with a 25 μm layer thickness.

The process parameters used in the design of experiment are summarised in Table 1. Cuboids of $7 \times 7 \times 4 \text{ mm}^3$ were

printed on a $90 \times 90 \text{ mm}^2$ 316 L substrate and cut from the substrate using electrical discharge machining (EDM). The small amount of powder blended resulted in a small print (4 mm height) therefore the samples were analysed in the XY plane. A second build was made with the recycled powder on a smaller $40 \times 40 \text{ mm}^2$ 316 L substrate. Cuboids of $5 \times 5 \times 10 \text{ mm}^3$ were printed, cut, and analysed in the build direction. The two builds were printed with a 25 μm layer thickness and are shown in Fig. 4b, c. The line energy density (E , J/mm^2) was calculated using the following equation:

$$E = \frac{P}{h * v} \quad (1)$$

,where P is the average laser power (W), h is the hatching distance (mm), and v is the scanning speed (mm/s).

2.3 Sample preparation and analysis

The samples were metallographically polished to a mirror-like finish and etched for less than 1 s with Kalling's II reagent to reveal the martensite twins. The relative density was evaluated through image analysis using ImageJ software. One of the samples with the highest relative density was heat-treated according to [29] by first homogenising them at 1060 $^{\circ}\text{C}$ for 12 h, followed by atomic ordering treatment at 800 $^{\circ}\text{C}$ for 4 h, after which the samples were furnace cooled to ambient temperature. The composition and homogeneity was evaluated by the aforementioned EDS system and by x-ray fluorescence (XRF) on 16 points

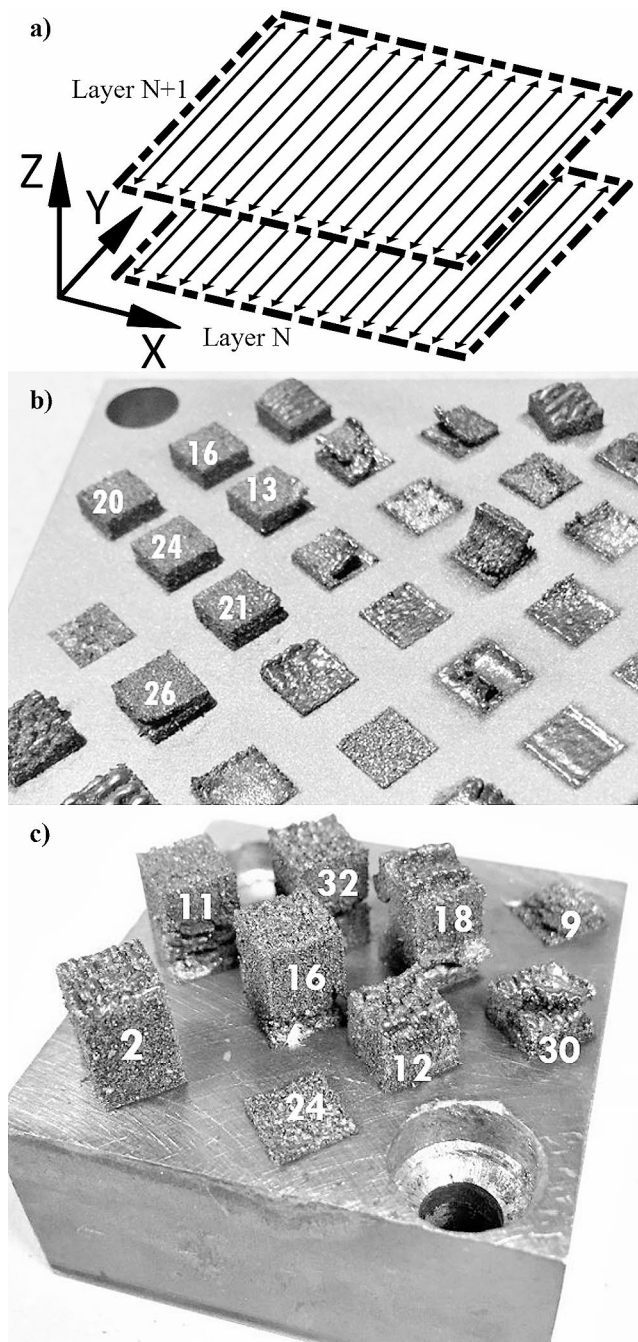


Fig. 4 (a) Unidirectional strategy used for building the samples, (b) the first batch of samples on the larger substrate, and (c) the second batch of samples on the smaller substrate. The labels correspond to the same sets of parameters (listed in Table 2) in both batch 1 and 2

Table 1 Summary of the used parameters

P (W)	v (mm/s)	h (μm)	E (J/mm^2)
100	1000	15	0.37-20
150	2000	45	
200	3000	90	
250			
300			

with an absolute accuracy of 0.3 at% using a X-Strata 960 (Oxford Instruments) analyser calibrated with a reference Ni-Mn-Ga sample of known composition. X-ray diffraction (XRD) measurements were performed using a PANalytical Empyrean 3 diffractometer (Co tube, $\lambda = 0.179031$ nm) equipped with parallel beam x-ray mirror optics for the incident beam, a PIXcel3D-Medipix3 detector (scanning line detector mode, 0.5° anti-scatter slit), and a zero-background sample holder. Differential scanning calorimetry (DSC) was conducted from 20 to 200 $^\circ\text{C}$ upon heating and cooling (DSC– 5 $^\circ\text{C}/\text{min}$ heating/cooling rate) on a Netzsch STA 449 F3 Jupiter to determine the phase transformation temperatures.

3 Results and discussion

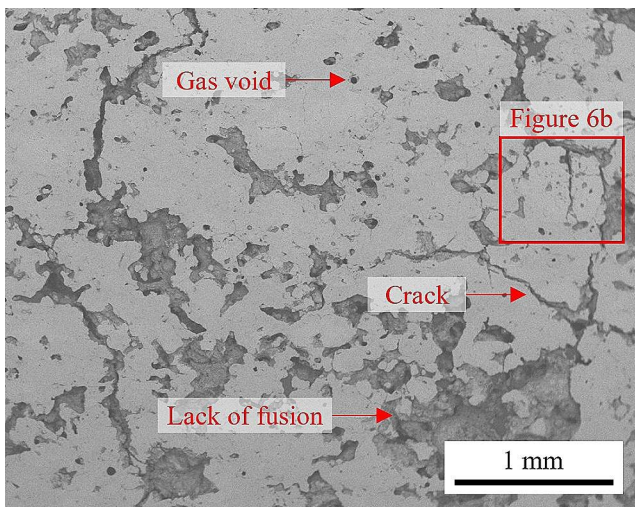
Figure 4 presents a picture of the two builds done with the powder blend. Only a limited set of parameters were effective in producing cubes. Samples with high energy density ($E > 4$ J/mm^2) overheated and delaminated while samples with low energy density ($E < 0.74$ J/mm^2) did not stick to the substrate due to lack of melting. The successful samples exhibited a high level of porosity (20–30%) with a rough surface finish. The second batch was conducted with the aim of controlling repeatability in taller samples, however, only one set of parameters from the first batch proved successful. This lack of repeatability can be attributed to the poor flowability of the powder blend, as Ga particles are larger in size compared to Ni and Mn particles. Samples 20 (250 W, 3000 mm/s, 45 μm) and 24 (150 W, 3000 mm/s, 45 μm) were successful in the first batch, but showed signs of delamination in the second, potentially due to an overheating caused by the larger height or insufficient wettability with the substrate. Another factor could be a smaller heat dissipation due to the smaller substrate in the second batch. Table 2 lists the parameters of the successful samples. A favourable energy density of around 1 J/mm^2 was observed, however, further optimisation of parameters is necessary to fully understand their individual impact.

Figure 5 shows a SEM image of the as-built sample 20 (250 W, 3000 mm/s, 45 μm). The figure highlights three distinct types of defects. Primarily, irregular porosity, attributed to lack of fusion, is observable. Additionally, small spherical pores, likely a result of element evaporation or trapped argon, are present. Cracks, a common occurrence in Ni-Mn-Ga samples, are widespread throughout the samples.

The XRF results presented in Table 3 demonstrate that the chemical composition of the sample is highly heterogeneous, with a significant variation of Ga observed throughout. Ga readily forms alloys with Mn and Ni, as evidenced by the presence of Ga-rich regions observed throughout

Table 2 Parameters of the selected samples built in the first and the second batch using the elemental powder blend. The numbering corresponds to the same set regardless the batch number

	Sample #	P (W)	v (mm/s)	h (μm)	E (J/mm^2)	Relative density (%)
Batch 1	13	200	3000	90	0.74	80.14
	16	300	3000	90	1.11	76.89
	20	250	3000	45	1.85	82.21
	21	100	3000	15	2.22	76.98
	24	150	3000	45	1.11	83.06
	26	150	2000	90	0.83	79.15
Batch 2	2	200	2000	45	2.22	-
	11	200	2000	90	1.11	-
	16	300	3000	90	1.11	-
	32	250	2000	90	1.39	-

**Fig. 5** SEM image of a cross section along the build direction of sample 20. Three types of defects are pointed as gas voids, lack of fusion and cracks. The red square corresponds to Fig. 6b**Table 3** Composition analysis (XRF) of sample 20 (250 W, 3000 mm/s, 45 μm) before and after heat-treatment

	<i>As-built</i>		
	Ni (at%)	Mn (at%)	Ga (at%)
Average	48.79	35.28	15.93
Standard deviation	4.40	2.81	6.28
Range	16.56	11.32	23.58
	<i>Heat-treated</i>		
	Ni (at%)	Mn (at%)	Ga (at%)
Average	50.63	36.43	12.94
Standard deviation	0.80	0.97	0.96
Range	2.80	3.53	3.35

sample 20 (250 W, 3000 mm/s, 45 μm). This is apparent in Fig. 6a, which was captured under an optical microscope and reveals dark needle structures. EDS analysis confirms the presence of Ga-Mn and Ga-Ni compounds. Segregations of Ni and Mn have also been noted in other areas, which may be a result of unmelted powders or insufficient heat input to blend the melt pool. The variation in Ga content is also related to the build layer thickness compared to the Ga

powder particles. According to Fig. 3, the second peak (corresponding to Ga particles) is approximately at 151.1 μm whereas the layer thickness used during printing was only 25 μm . Consequently, the recoater may push some of the larger Ga particles from the build plate, which can result in selective removal of Ga from the blend. Additionally, some Ga particles may melt prematurely due to the heat accumulation during L-PBF, which may also contribute variation of the Ga content and formed microstructures locally within the sample.

Heat treatment resulted in elemental diffusion and the subsequent increase in chemical homogeneity. Despite this improvement, however, the standard deviation remains substantial when compared to experiments using pre-alloyed powder [19]. Specifically, the standard deviation here is on the order of 1 at% when using a powder blend, whereas when using pre-alloyed powders, it is on the order of 0.1 at% while previous studies have established that achieving final homogeneity is critical to observe a MFIS. To further improve homogeneity, several L-PBF process related approaches could be adopted, such as using slower scanning speed and/or lower laser power, using double scanning, or the implementation of a heated platform during the fabrication process. These methods would allow for longer exposure and reduction of the thermal gradients, ultimately helping to dissolve the chemical segregations and therefore, further enhancing homogeneity. Another approach would be to use pre-alloyed Ga. Preferably Ni-Ga as the Mn is the element which the composition is the most likely to fluctuate and would be easier to control as an elemental powder.

Figure 7 shows the x-ray diffractograms obtained at ambient temperature for sample 20 (250 W, 3000 mm/s, 45 μm) before and after heat-treatment. By examining the diffraction peaks present in the samples, we were able to identify the crystalline phases and determine their average lattice parameters, as shown in Table 4.

The lattice parameters of seven-layered modulated (14 M) orthorhombic and non-modulated (NM) tetragonal martensites are presented in the coordinate system of

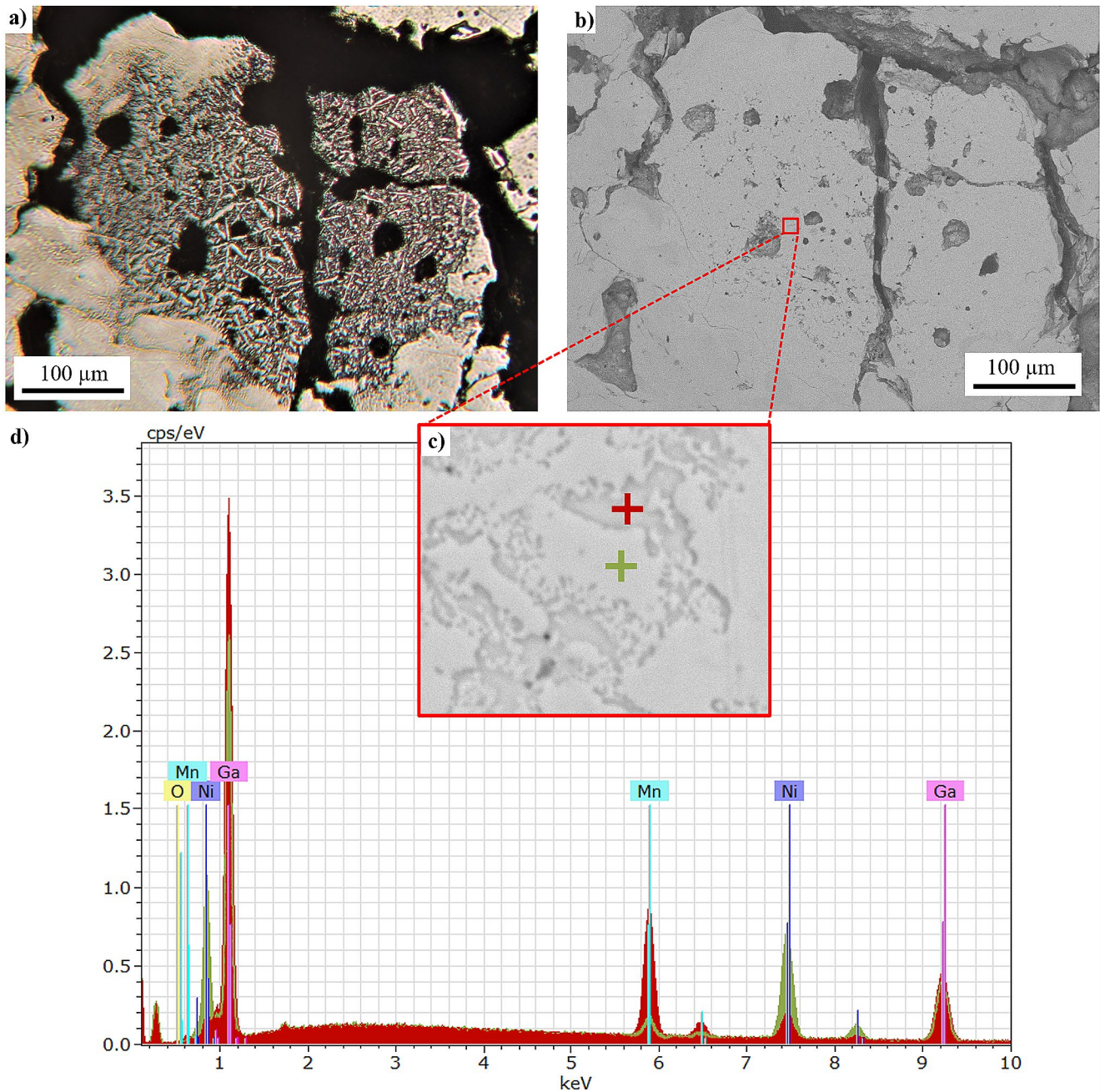


Fig. 6 (a) An optical micrograph, (b, c) SEM images, and (d) EDS analysis of a Ga-rich region in the XY plane. (d) Ga-Mn compound is shown in red and a Ga-Ni compound in green

the parent phase (cubic $L2_1$ austenite). Only the main diffraction peaks were considered in calculating the lattice parameters. The as-built sample exhibited a complex diffraction pattern with a large quantity of peaks originating from multiple different crystalline phases. After conducting a thorough examination, it was determined that most of the peaks belonged to the MnO and cubic $L2_1$ austenite phases. Nonetheless, some low-intensity peaks indicate the presence of Ni-rich γ phase and 14 M martensite in the

sample. The 14 M peaks' relatively low intensity compared to the background noise made it impossible to estimate the monoclinic angle, resulting in the use of an orthorhombic approximation with a gamma-angle of 90° to calculate the phase's lattice parameters. Foremost, the presence of multiple crystalline phases was expected based on the large compositional variations observed in the sample using XRF. The existence of the γ phase can be attributed to the presence of the Ni-rich segregations within the as-built sample, whereas

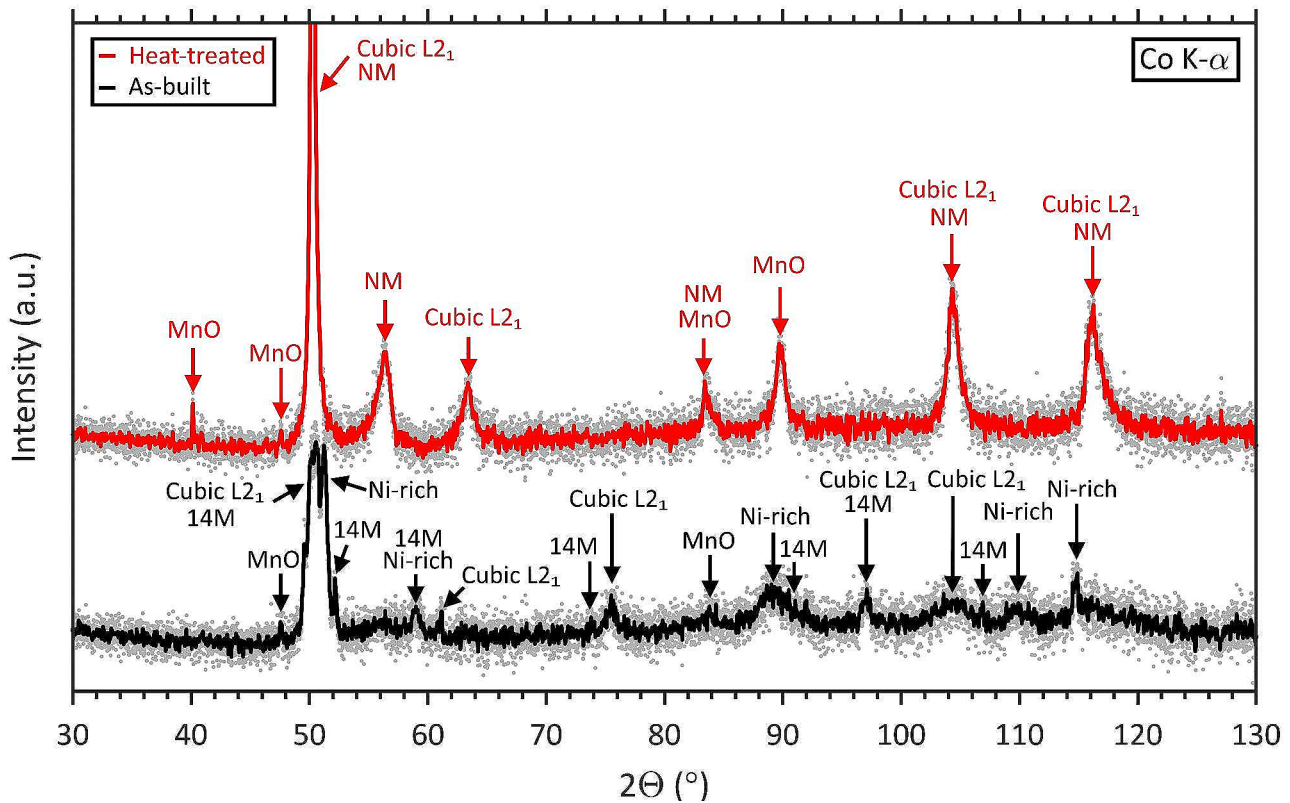


Fig. 7 XRD diffractograms of sample 20 (250 W, 3000 mm/s, 45 μm) in as built and heat-treated conditions

Table 4 Approximate lattice parameters of the crystalline phases detected from the sample 20 (250 W, 3000 mm/s, 45 μm) before and after heat-treatment. All lattice parameters are presented with an approximate accuracy of ± 0.02 \AA

Phase	As-built			Heat-treated		
	a (\AA)	b (\AA)	c (\AA)	a (\AA)	b (\AA)	c (\AA)
MnO	4.44	4.44	4.44	4.44	4.44	4.44
Ni-rich	3.62	3.62	3.62	-	-	-
Cubic L ₂₁	5.85	5.85	5.85	5.93	5.93	5.93
14 M	6.06	5.90	5.50	-	-	-
NM	-	-	-	5.38	5.38	6.65

MnO was likely introduced into the sample as surface oxides of the used Mn-powder prior to L-PBF. Additionally, the presence of multiple phases can be partially attributed to the inherent chemical composition inhomogeneity that typically occurs in the anisotropic microstructures developed during L-PBF. The heat-treated sample exhibited a markedly different diffraction pattern, as the peaks originating from the 14 M martensite and Ni-rich γ phases were no longer present, and instead, the diffraction peaks originating from NM martensite were observed. As mentioned in the XRF section, heat treatment at 1060 $^{\circ}\text{C}$ for 12 h resulted in significant chemical homogenisation, effectively dissolving the 14 M martensite and Ni-rich γ phase. The heat-treated sample was primarily composed of the cubic L₂₁ austenite, NM martensite and the previously observed MnO. The sample displayed a little variation in the lattice parameters of

MnO, which was expected due to its relatively high melting temperature of 1842 $^{\circ}\text{C}$ [30], preventing it from dissolving during the heat treatment. The presence of Mn-oxide is most likely to pin the twin boundary motion and cancel the MSM effect. Additionally, the final composition of the heat-treated sample is largely deviated from the ideal compositions [5] for obtaining large MFIS. However, the advantage of in-situ alloying is that the composition could be easily tuned by adapting the proportions of the elemental powders.

Sample 20 (250 W, 3000 mm/s, 45 μm) was inspected using optical microscopy and SEM before and after heat-treatment (Fig. 8). The relative density of the as-built sample 20 was determined to be $\sim 70\%$ using image analysis. Upon etching, the as-built sample exhibited stripe-like patterns associated with martensitic twins, consistent with the XRD analysis that identified the presence of 14 M martensite in

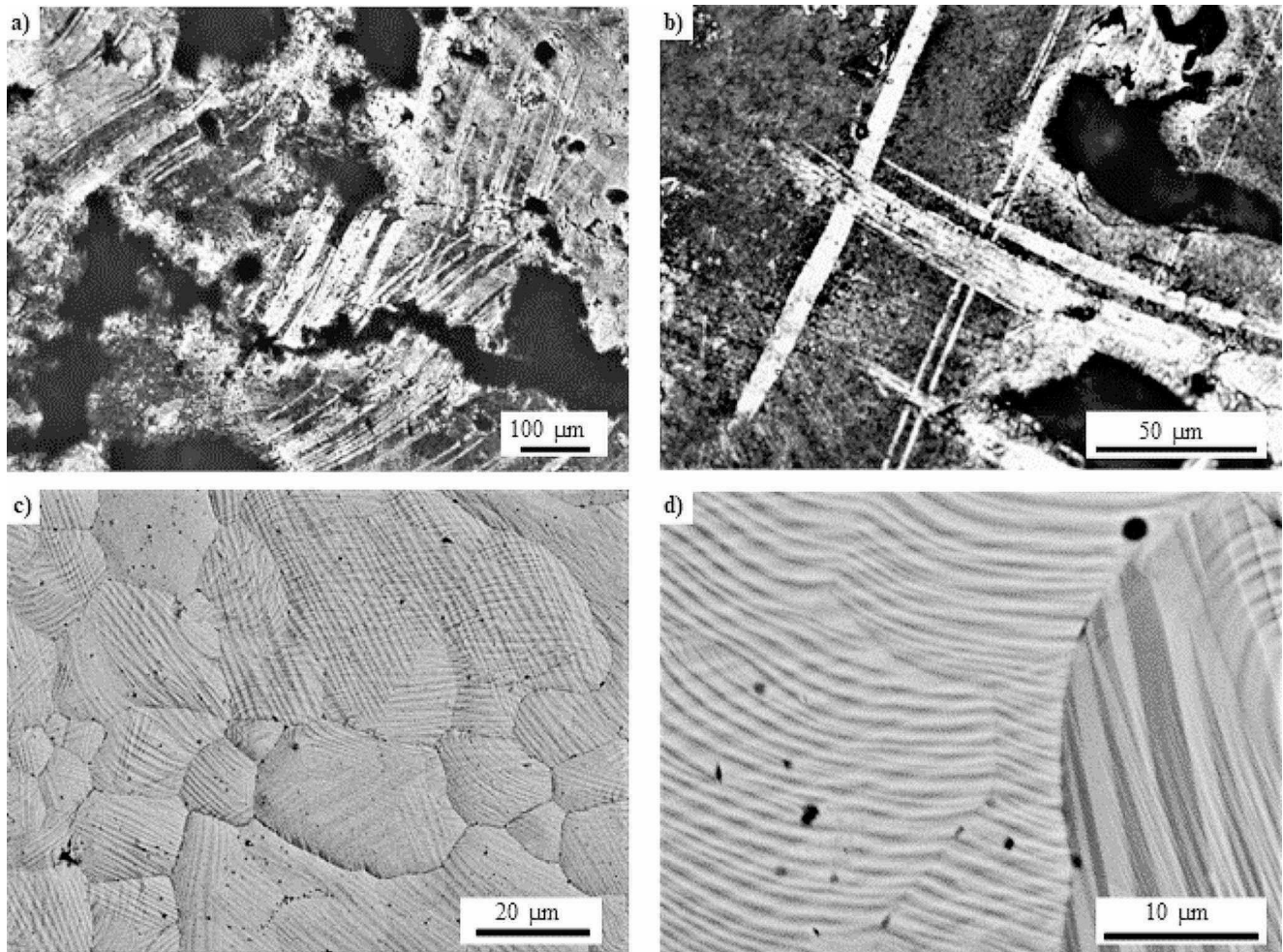


Fig. 8 (a, b) Optical micrographs showing twins in as-built sample 20 (250 W, 3000 mm/s, 45 μm), and (c, d) SEM micrographs showing grains and twins in heat-treated sample 20

the sample. No segregation can be seen in Fig. 8. Following heat treatment, the grain structure of the sample was more clearly observed, consisting predominantly of equiaxed grains with an average size of 62 nm. Each grain exhibited a distinct martensite twin structure, consistent with the XRD results indicating a predominantly martensitic (NM phase) in the heat-treated sample, with some twins spanning grain boundaries. These findings suggest a high degree of chemical homogenisation and recrystallisation of the microstructure. EDS analysis of various regions of the heat-treated sample showed no evidence of element segregation. However, DSC analysis before and after heat treatment did not reveal any distinct phase transformations. Despite the absence of discernible segregation in the EDS analysis and the SEM observations, the XRD analysis showed that the sample was not crystallographically uniform after heat treatment. The presence of multiple crystal structures and

chemical heterogeneities (as shown by XRF results) effectively hinders the detection of the phase transformations in the DSC results.

4 Conclusion

This research represents a preliminary investigation of Ni-Mn-Ga manufactured using L-PBF from a blend of elemental powders. Despite the significant differences between the elemental powders and liquid Ga, the results are promising. The microstructure features distinctive stripe patterns originating from the 14 M crystallographic structure, as confirmed by XRD analysis. Although heat-treatment improved chemical homogeneity, and dissolved the Ni-rich phase, it was unable to dissolve the MnO phase, which impedes the shape memory effect. Further studies should focus on dissolving the segregations through adapted heat treatment, different scanning strategy, double scanning, or pre-alloying

of two elements such as Ni-Ga or Ni-Mn. Furthermore, the in-situ alloying process provides the opportunity to explore adding additional elements such as Co, Cu, Cr or Fe [31] to reduce segregation through alloying with Ni.

Supplementary Information The online version contains supplementary material available at <https://doi.org/10.1007/s40964-024-00589-x>.

Acknowledgements This work was financially supported by the Defence Science and Technology Laboratory (DSTL), the Strategic Research Council of Finland (grant number 313349), the Academy of Finland (grant number 325910), and the AMBI (Analytics-based Management for Business and Manufacturing Industry) research platform of Lappeenranta-Lahti University of Technology LUT.

Declarations

Conflict of interest On behalf of all authors, the corresponding author states that there is no conflict of interest.

Open Access This article is licensed under a Creative Commons Attribution 4.0 International License, which permits use, sharing, adaptation, distribution and reproduction in any medium or format, as long as you give appropriate credit to the original author(s) and the source, provide a link to the Creative Commons licence, and indicate if changes were made. The images or other third party material in this article are included in the article's Creative Commons licence, unless indicated otherwise in a credit line to the material. If material is not included in the article's Creative Commons licence and your intended use is not permitted by statutory regulation or exceeds the permitted use, you will need to obtain permission directly from the copyright holder. To view a copy of this licence, visit <http://creativecommons.org/licenses/by/4.0/>.

References

- Ullakko K, Huang JK, Kantner C, O'Handley RC, Kokorin VV (1996) Large magnetic-field-induced strains in Ni₂MnGa single crystals. *Appl Phys Lett* 69:1966–1968. <https://doi.org/10.1063/1.117637>
- Murray SJ, Marioni M, Allen SM, O'Handley RC, Lograsso TA (2000) 6% magnetic-field-induced strain by twin-boundary motion in ferromagnetic Ni-Mn-Ga. *Appl Phys Lett* 77:886–888. <https://doi.org/10.1063/1.1306635>
- Sozinov A, Likhachev AA, Lanska N, Ullakko K (2002) Giant magnetic-field-induced strain in NiMnGa seven-layered martensitic phase. *Appl Phys Lett* 80:1746–1748. <https://doi.org/10.1063/1.1458075>
- Sozinov A, Lanska N, Soroka A, Zou W (2013) 12% magnetic field-induced strain in Ni-Mn-Ga-based non-modulated martensite. *Appl Phys Lett* 102. <https://doi.org/10.1063/1.4775677>
- Laitinen V, Saren A, Sozinov A, Ullakko K (2021) Giant 5.8% magnetic-field-induced strain in additive manufactured Ni-Mn-Ga magnetic shape memory alloy. *Scr Mater* 208:114324. <https://doi.org/10.1016/j.scriptamat.2021.114324>
- Chmielus M, Zhang XX, Witherspoon C, Dunand DC, Müllner P (2009) Giant magnetic-field-induced strains in polycrystalline Ni-Mn-Ga foams. *Nat Mater* 8:863–866. <https://doi.org/10.1038/nmat2527>
- Caputo MP, Berkowitz AE, Armstrong A, Müllner P, Solomon CV (2018) Addit Manuf 21:579–588. <https://doi.org/10.1016/j.addma.2018.03.028>. 4D printing of net shape parts made from Ni-Mn-Ga magnetic shape-memory alloys
- Caputo MP, Solomon CV (2017) A facile method for producing porous parts with complex geometries from ferromagnetic Ni-Mn-Ga shape memory alloys. *Mater Lett* 200:87–89. <https://doi.org/10.1016/j.matlet.2017.04.112>
- Mostafaei A, De Vecchis PR, Stevens EL, Chmielus M (2018) Sintering regimes and resulting microstructure and properties of binder jet 3D printed Ni-Mn-Ga magnetic shape memory alloys. *Acta Mater* 154:355–364. <https://doi.org/10.1016/j.actamat.2018.05.047>
- Mostafaei A, Kimes KA, Stevens EL, Toman J, Krimer YL, Ullakko K, Chmielus M (2017) Microstructural evolution and magnetic properties of binder jet additive manufactured Ni-Mn-Ga magnetic shape memory alloy foam. *Acta Mater* 131:482–490. <https://doi.org/10.1016/j.actamat.2017.04.010>
- Taylor SL, Shah RN, Dunand DC (2018) Ni-Mn-Ga microtrusses via sintering of 3D-printed inks containing elemental powders. *Acta Mater* 143:20–29. <https://doi.org/10.1016/j.actamat.2017.10.002>
- Taylor SL, Shah RN, Dunand DC (2019) Microstructure and porosity evolution during sintering of Ni-Mn-Ga wires printed from inks containing elemental powders. *Intermetallics* 104:113–123. <https://doi.org/10.1016/j.intermet.2018.10.024>
- Toman J, Müllner P, Chmielus M (2018) Properties of as-deposited and heat-treated Ni-Mn-Ga magnetic shape memory alloy processed by directed energy deposition. *J Alloys Compd* 752:455–463. <https://doi.org/10.1016/j.jallcom.2018.04.059>
- Nilsén F, Ituarte IF, Salmi M, Partanen J, Hannula SP (2019) Effect of process parameters on non-modulated Ni-Mn-Ga alloy manufactured using powder bed fusion. *Addit Manuf* 28:464–474. <https://doi.org/10.1016/j.addma.2019.05.029>
- Laitinen V, Sozinov A, Saren A, Salminen A, Ullakko K (2019) Laser powder bed fusion of Ni-Mn-Ga magnetic shape memory alloy. *Addit Manuf* 30:100891. <https://doi.org/10.1016/j.addma.2019.100891>
- Milleret A, Laitinen V, Ullakko K, Fenineche N, Attallah MM (2022) Laser powder bed fusion of (14 M) Ni-Mn-Ga magnetic shape memory alloy lattices. *Addit Manuf* 60:1–14. <https://doi.org/10.1016/j.addma.2022.103231>
- Saren A, Laitinen V, Vinogradova M, Ullakko K (2023) Twin boundary mobility in additive manufactured magnetic shape memory alloy 10 M Ni-Mn-Ga. *Acta Mater* 246:118666. <https://doi.org/10.1016/j.actamat.2022.118666>
- Ullakko K, Laitinen V, Saren A, Sozinov A, Musiienko D, Chmielus M, Salminen A (2018) Ni-Mn-Ga Actuating Elements Manufactured Using 3D Printing, 11th Eur. Symp. Martensitic Transform. https://www.researchgate.net/publication/329556511_Ni-Mn-Ga_Actuating_Elements_Manufactured_Using_3D_Printing
- Milleret A, Laitinen V, Ullakko K, Fenineche N, Attallah MM (2022) Laser powder bed fusion of (14 M) Ni-Mn-Ga magnetic shape memory alloy lattices. *Addit Manuf* 60:103231. <https://doi.org/10.1016/j.addma.2022.103231>
- Niendorf T, Brenne F, Krooß P, Vollmer M, Günther J, Schwarze D, Biermann H (2016) *Metall Mater Trans Phys Metall Mater Sci* 47:2569–2573. <https://doi.org/10.1007/s11661-016-3412-z>. Microstructural Evolution and Functional Properties of Fe-Mn-Al-Ni Shape Memory Alloy Processed by Selective Laser Melting
- Dunand DC, Müllner P (2011) Size effects on magnetic actuation in Ni-Mn-Ga shape-memory alloys. *Adv Mater* 23:216–232. <https://doi.org/10.1002/adma.201002753>

22. Milleret A (2022) 4D printing of Ni–Mn–Ga magnetic shape memory alloys: a review. *Mater Sci Technol* 1–14. <https://doi.org/10.1080/02670836.2022.2062655>
23. Lanska N, Söderberg O, Sozinov A, Ge Y, Ullakko K, Lindroos VK (2004) Composition and temperature dependence of the crystal structure of Ni–Mn–Ga alloys. *J Appl Phys* 95:8074–8078. <https://doi.org/10.1063/1.1748860>
24. Zheng P, Lindquist P, Yuan B, Müllner P, Dunand DC (2014) Fabricating Ni–Mn–Ga microtubes by diffusion of Mn and Ga into Ni tubes. *Intermetallics* 49:70–80. <https://doi.org/10.1016/j.intermet.2014.01.014>
25. Gaitzsch U, Drache J, McDonald K, Müllner P, Lindquist P (2012) Obtaining of Ni–Mn–Ga magnetic shape memory alloy by annealing electrochemically deposited Ga/Mn/Ni layers. *Thin Solid Films* 522:171–174. <https://doi.org/10.1016/j.tsf.2012.08.019>
26. Knieps MS, Reynolds WJ, Dejaune J, Clare AT, Evirgen A (2021) In-situ alloying in powder bed fusion: the role of powder morphology. *Mater Sci Eng A* 807:140849. <https://doi.org/10.1016/j.msea.2021.140849>
27. Ewald S, Kies F, Hermsen S, Voshage M, Haase C, Schleifenbaum JH (2019) Rapid Alloy Development of extremely high-alloyed Bed Fusion, materials (Basel). 1–15
28. Laitinen V, Salminen A, Ullakko K (2019) First investigation on processing parameters for laser powder bed fusion of Ni–Mn–Ga magnetic shape memory alloy. *J Laser Appl* 31:022303. <https://doi.org/10.2351/1.5096108>
29. Laitinen V, Sozinov A, Saren A, Chmielus M, Ullakko K (2021) Characterization of as-built and heat-treated Ni–Mn–Ga magnetic shape memory alloy manufactured via laser powder bed fusion. *Addit Manuf* 39:101854. <https://doi.org/10.1016/j.addma.2021.101854>
30. Haynes WM (1942) *CRC Handbook of Chemistry and Physics*. 97th Edition
31. Namvari M, Laitinen V, Sozinov A, Saren A, Ullakko K (2023) Effects of 1 at.% additions of Co, Fe, Cu, and Cr on the properties of Ni–Mn–Ga-based magnetic shape memory alloys. *Scr Mater* 224:115116. <https://doi.org/10.1016/j.scriptamat.2022.115116>

Publisher's Note Springer Nature remains neutral with regard to jurisdictional claims in published maps and institutional affiliations.